

Article

CdS Nanoparticles Decorated 1D CeO₂ Nanorods for Enhanced Photocatalytic Desulfurization Performance

Xiaowang Lu ^{1,*}, Zhengwei Liu ¹, Xiangping Zhao ¹, Weiye Xu ¹, Haijun Hou ¹ and Junchao Qian ²¹ School of Material Science and Engineering, Yancheng Institute of Technology, Yancheng 224051, China² School of Material Science and Engineering, Suzhou University of Science and Technology, Suzhou 215009, China

* Correspondence: luxiaowang@ycit.edu.cn

Abstract: CdS nanoparticles were constructed onto one-dimensional (1D) CeO₂ nanorods by a two-step hydrothermal method. The X-ray diffraction (XRD), transmission electron microscopy (TEM), Raman spectra, X-ray photoelectron spectra (XPS) and UV-Vis diffuse reflection spectroscopy (DRS) techniques were used to characterize these CdS/CeO₂ nanocomposites. It was concluded that when the molar ratio of CdS and CeO₂ was 1:1, the nanocomposites exhibited the best photocatalytic desulfurization activity, reaching 92% in 3 h. Meanwhile, transient photocurrent (PT) measurement, photoluminescence (PL) spectra and electrochemical impedance spectroscopy (EIS) measurement indicated that the modification of CeO₂ nanorods by CdS nanoparticles could significantly inhibit the recombination of photogenerated electrons and holes. In addition, the possible mechanism of photocatalytic oxidation desulfurization of the nanocomposites was proposed. This study may provide an effective CeO₂-based photocatalyst for photocatalytic desulfurization applications.

Keywords: CdS; CeO₂; nanocomposite; heterojunction; photocatalytic desulfurization

Citation: Lu, X.; Liu, Z.; Zhao, X.; Xu, W.; Hou, H.; Qian, J. CdS Nanoparticles Decorated 1D CeO₂ Nanorods for Enhanced Photocatalytic Desulfurization Performance. *Catalysts* **2022**, *12*, 1478. <https://doi.org/10.3390/catal12111478>

Academic Editor: Gilles Berhault

Received: 16 October 2022

Accepted: 17 November 2022

Published: 19 November 2022

Publisher's Note: MDPI stays neutral with regard to jurisdictional claims in published maps and institutional affiliations.



Copyright: © 2022 by the authors. Licensee MDPI, Basel, Switzerland. This article is an open access article distributed under the terms and conditions of the Creative Commons Attribution (CC BY) license (<https://creativecommons.org/licenses/by/4.0/>).

1. Introduction

Sulfur oxides (SO_x) emitted from vehicle fuel combustion have been shown to cause acid rain and haze, which has become a serious environmental pollution problem. Therefore, it is urgent to remove sulfur-containing organic compounds from fuel to reduce sulfur content [1,2]. Subsequently, a series of desulfurization technologies have been developed, such as hydrodesulfurization [3], oxidative desulfurization [4], adsorptive desulfurization [5] and biodesulfurization [6]. Among them, hydrodesulfurization is the predominant technology currently used in industry, which requires hydrogen consumption to achieve a high pressure and high temperature. In addition, it is difficult to remove dibenzothio- phene (DBT) and its derivatives from fuel. Alternatively, photocatalytic desulfurization is a new desulfurization technology using a semiconductor photocatalyst for catalytic oxidation desulfurization, which has the advantages of mild reaction conditions, low energy consumption and environmental friendliness. In the process of photocatalytic desulfurization, DBT and its derivatives can be oxidized to corresponding sulfones, which have polarity and can be easily removed by solvent extraction [7,8]. In recent years, a series of photocatalytic desulfurization catalysts have been developed, such as a TiO₂-based photocatalyst [9,10], bismuth series material [11,12], g-C₃N₄ framework material [13,14], metal organic framework material [15], etc.

CeO₂ is an important rare earth oxide semiconductor material, which is commonly used as a photocatalyst for pollutant degradation and energy conversion. However, CeO₂ is a wide band gap semiconductor, which usually responds in the ultraviolet region, and ultraviolet light only accounts for 5% of the sunlight, which greatly hinders its application [16–18]. Therefore, the heterojunction of CeO₂ and another narrow band gap semiconductor is expected to improve the photocatalytic performance. Moreover, one-dimensional (1D) nanomaterials have attracted much attention in recent years due to their

high length-to-diameter ratio, which facilitates the rapid charge transfer along the axial direction [19,20].

CdS is a narrow band gap semiconductor, which can effectively use visible light and is a promising material. Nevertheless, the rapid recombination of photogenerated carriers and severe photocorrosion hinder the further application of CdS [21,22]. Thus, the effective combination of CdS and CeO₂ to form a heterojunction is expected to overcome these disadvantages.

Herein, in this work, we used CdS nanoparticles to decorate 1D CeO₂ nanorods to prepare a well-defined interfacial heterojunction composite. Then the photocatalytic performance of the prepared photocatalysts was investigated by the photocatalytic degradation of dibenzothiophene (DBT) under visible irradiation. Finally, the enhancement mechanism of photocatalytic desulfurization was studied.

2. Results

2.1. Preparation of Samples

2.1.1. Synthesis of CeO₂ Nanorods

A total of 0.02 mol Ce (NO₃)₃ · 6H₂O was dissolved in 5 mL deionized water, and then 35 mL 10 M NaOH solution was added. After being fully stirred, the mixture was transferred to a 50 mL Teflon hydrothermal reactor and heated to 110 °C for 10 h; the obtained products were centrifugally washed and dried, and then calcined at 400 °C for 2 h to obtain CeO₂ nanorods.

2.1.2. Synthesis of CdS/CeO₂ Composite

A certain amount of prepared CeO₂ nanorod powders were ultrasonically dispersed in 20 mL of deionized water, and then 20 mL of 0.1 M CdCl₂ · 2.5H₂O solution was added. After full stirring, 20 mL of 0.1 M Na₂S solution was slowly added, and then the mixture was transferred to a Teflon hydrothermal reactor and heated to 160 °C for 24 h; then the suspension was filtered, washed and dried to finally obtain the CdS/CeO₂ composite. The molar ratios of CdS to CeO₂ in the prepared samples were 1:2, 1:1 and 2:1, respectively.

2.2. Characterization

X-ray diffraction (XRD) measurement was performed on an X-ray diffractometer with Cu K α radiation (Rigaku, D/max-RB, λ = 0.15406 nm); Raman spectra were measured by a Thermo Fisher Scientific DXR Raman spectrophotometer and the excitation laser wave length was 532 nm. The morphology was observed by a JEOL JEM-2100 transmission electron microscope (TEM) equipped with Gatan 832 CCD operating at a voltage of 200 kV; X-ray photoelectron spectroscopy (XPS) analysis was carried out using a Thermo Fisher Scientific ESCALAB 250 spectrometer with the mono Al K α radiation (1486.6 eV). Photoluminescence (PL) spectra were collected on a PerkinElmer LS45 fluorescence spectrometer with an excitation wavelength of 400 nm; ultraviolet–visible diffuse reflectance spectra (UV-Vis DRS) were measured by a Shimadzu UV-2450 spectrophotometer equipped with an integrating sphere.

2.3. Photoelectrochemical Measurements

The photoelectrochemical tests were carried out on an LK5600 photoelectrochemical workstation. For the photocurrent measurement, the prepared sample was deposited on the surface of FTO glass as the working electrode, the Ag/AgCl electrode as the reference electrode, the Pt plate as the counter electrode and the 0.1 M Na₂SO₄ solution as the supporting electrolyte, and the 300 W xenon lamp as the light source. For electrochemical impedance spectroscopy (EIS) measurements, the three electrodes system was also used. The electrolyte solution was 0.5 M KCl solution containing 0.01 M K₃Fe(CN)₆/K₄Fe(CN)₆ (molar ratio 1:1), performed at bias voltages 0.5 V, in the frequency range of 0.1 Hz–100 kHz with oscillation potential amplitudes of 0.01 V at room temperature.

2.4. Photocatalytic Desulfurization Measurement

A total of 0.08 g DBT was dissolved in 200 mL n-octane as model oil; subsequently, a 0.1 g photocatalyst was added under constant stirring, and then appropriate H_2O_2 was added (molar ratio of O/S = 4:1). After dark adsorption for 30 min, the photocatalytic desulfurization process was carried out in a photochemical reaction instrument with a xenon lamp (300 W, with ultraviolet cut-off filter ($\lambda > 420$ nm)). The dispersion was collected every 30 min and extracted with acetonitrile, and the sulfur content was determined on a UV fluorescent sulfur analyzer. The desulfurization rate D (%) was obtained according to the following formula: $D = (1 - C_t/C_0) \times 100\%$, where C_0 is the initial sulfur content and C_t is the sulfur content of the solution at reaction time t .

3. Discussion

3.1. XRD Patterns Analysis

The structures of the samples are confirmed by XRD analysis in Figure 1. The characteristic diffraction peaks at 28.6° , 33.1° , 47.4° and 56.2° correspond to the (111), (200), (220) and (311) different crystal planes of cubic fluorite CeO_2 , respectively (JCPDS 34-0394). And the diffraction peaks at 24.6° , 26.4° , 28.0° , 36.5° , 43.6° , 47.7° and 51.7° are indexed to the (100), (002), (101), (102), (110), (103) and (112) crystal planes of the hexagonal structure CdS, respectively (JCPDS:41-1049). In addition, when CdS nanoparticles are deposited on CeO_2 nanorods, the characteristic peaks of both cubic fluorite CeO_2 and hexagonal CdS are observed in the composites. It is worth noting that by increasing the molar ratio of CdS to CeO_2 , the intensity of the characteristic peaks of CdS are enhanced in the composites. The results demonstrate that the CdS is successfully loaded on the surface of CeO_2 .

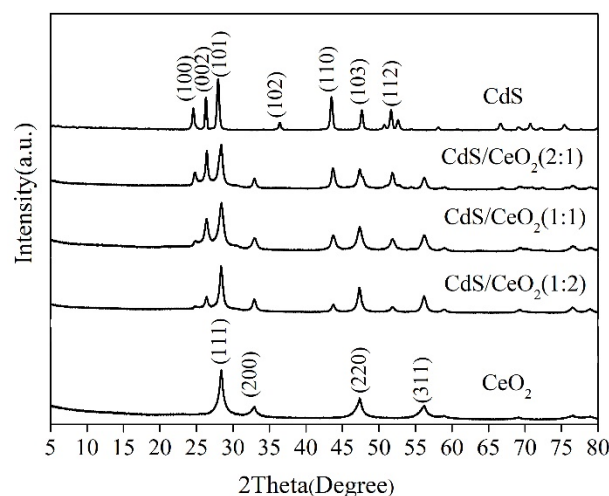


Figure 1. XRD patterns of CdS, CeO_2 and the various CdS/ CeO_2 composites.

3.2. Raman Spectroscopy Analysis

Raman spectroscopy with an excitation wavelength of 532 nm was used to measure the structure and electronic properties of the materials. As shown in Figure 2, for pure CeO_2 , the peak at 465 cm^{-1} can be attributed to the F2g Raman active interior phonon mode of the fluorite cubic structure [23]. As for pure CdS, the two dominant peaks at 300 cm^{-1} and 600 cm^{-1} are attributed to the first-order longitudinal optical (1LO) and the second-order longitudinal optical (2LO) phonon modes of CdS, respectively [24]. Moreover, it can be observed that all the composites have peaks corresponding to both CeO_2 and CdS with varying intensities. The Raman peak intensity of the CdS/ CeO_2 composites is lower than that of pure CeO_2 or pure CdS. This may be attributed to the scattering loss caused by defects in the heterojunction [25,26]. With the increase in CeO_2 content, the characteristic peak intensity of CeO_2 in the CdS/ CeO_2 composite gradually increases.

Therefore, the Raman measurement results further demonstrate the existence of CdS and CeO₂ in the composite.

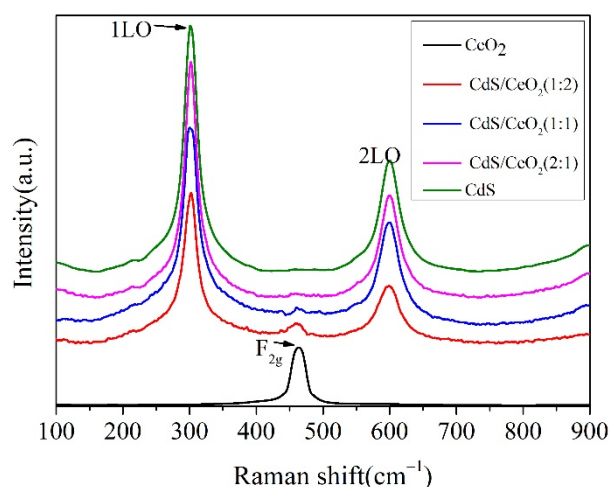


Figure 2. Raman spectra of CdS, CeO₂ and various CdS/CeO₂ samples.

3.3. Morphological Analysis

Figure 3 shows TEM and HRTEM images of CeO₂ nanorods and the CdS/CeO₂(1:1) composite. It can be seen from Figure 3a that the prepared CeO₂ presents a rod-like structure, with a diameter of 20–30 nm and a length of 50–100 nm. Moreover, the corresponding HRTEM image (Figure 3b) shows that the crystal plane spacing $d = 0.31$ nm corresponds to the (111) crystal plane of cubic fluorite CeO₂. As shown in Figure 3c, CdS nanoparticles are deposited on the surface of CeO₂ nanorods, and the structure of the CeO₂ nanorods is not destroyed in the composite. It can be seen from Figure 3d that the two different crystal plane spacings are $d = 0.315$ nm and $d = 0.31$ nm, which, respectively, correspond to the (101) crystal plane of hexagonal CdS and the (111) crystal plane of cubic fluorite CeO₂. The well-defined heterojunction structure may facilitate the separation of photogenerated electrons and holes, improving the photocatalytic efficiency.

3.4. XPS Spectra Analysis

The surface chemical states of the prepared samples are studied by XPS spectroscopy. The high-resolution XPS spectra of Ce 3d, O 1s, Cd 3d and S 2p are shown in Figure 4a–d, respectively. In Figure 4a, the characteristic peaks of Ce 3d are divided into eight fitting peaks, with the six peaks labeled as v_1 , v_2 , v_3 , u_1 , u_2 and u_3 representing Ce⁴⁺, and the other two peaks labeled as v_1 and u_1 corresponding to Ce³⁺, which indicates the presence of mixed Ce⁴⁺ and Ce³⁺ states in the samples [27]. According to the charge neutrality condition, the appearance of Ce³⁺ is an indicator of oxygen vacancies in CeO₂. The binding energy peaks labeled at 529.6 eV, 530.6 eV and 531.7 eV correspond to lattice oxygen (OL), oxygen vacancies (V_O) and chemisorbed oxygen (OA) in CeO₂ nanorods, respectively (Figure 4b). Therefore, it indicates that there is a certain amount of V_O in CeO₂. When CdS is loaded, all Ce 3d and O_L peaks shift slightly, indicating that there is charge transfer between CeO₂ and CdS [28,29]. As can be seen in Figure 4c, the peaks at 404.7 eV and 411.6 eV correspond to the Cd 3d_{5/2} and Cd 3d_{3/2} of Cd (II) states in the CdS sample. As shown in Figure 4d, the XPS spectrum of S 2p exhibits two peaks at 161.5 and 162.6 eV, which are attributed to S 2p_{3/2} and S 2p_{1/2}, respectively [30,31]. It is worth noting that the peaks of Ce 3d, O 1s, Cd 3d and S 2p are shifted slightly in CdS/CeO₂(1:1) compared with pure CeO₂ nanorods and CdS, indicating that a heterojunction is formed between CdS nanoparticles and CeO₂ nanorods, which is conducive to the effective separation of photogenerated electrons and holes.

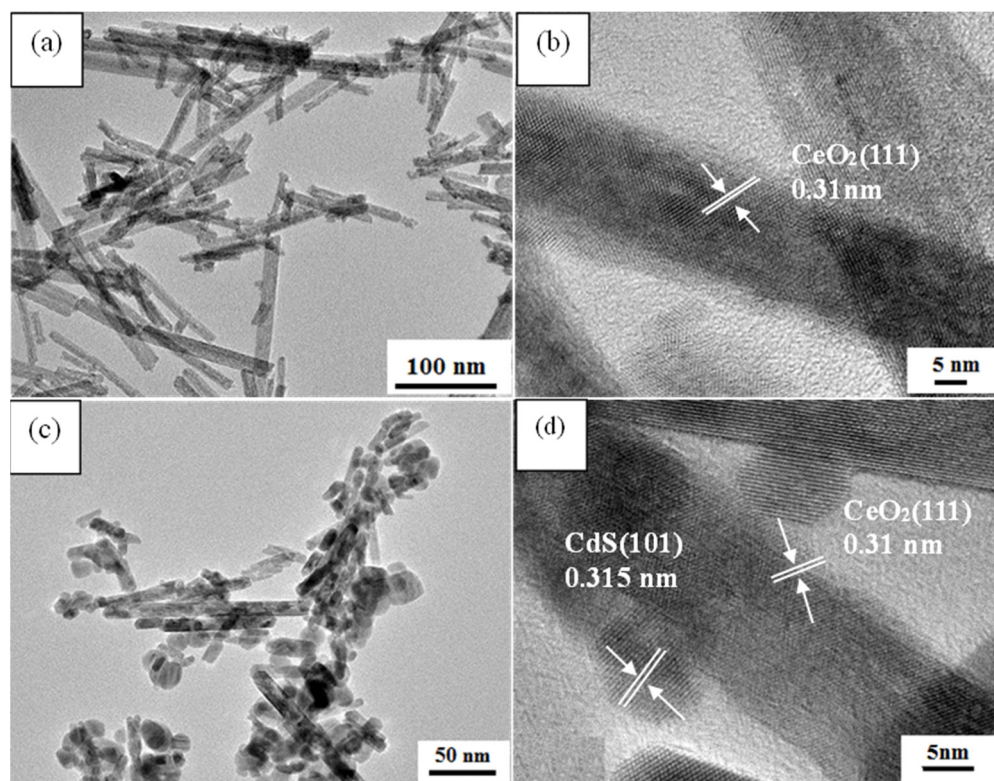


Figure 3. TEM and HRTEM images of CeO_2 (a,b) and $\text{CdS}/\text{CeO}_2(1:1)$ composite (c,d).

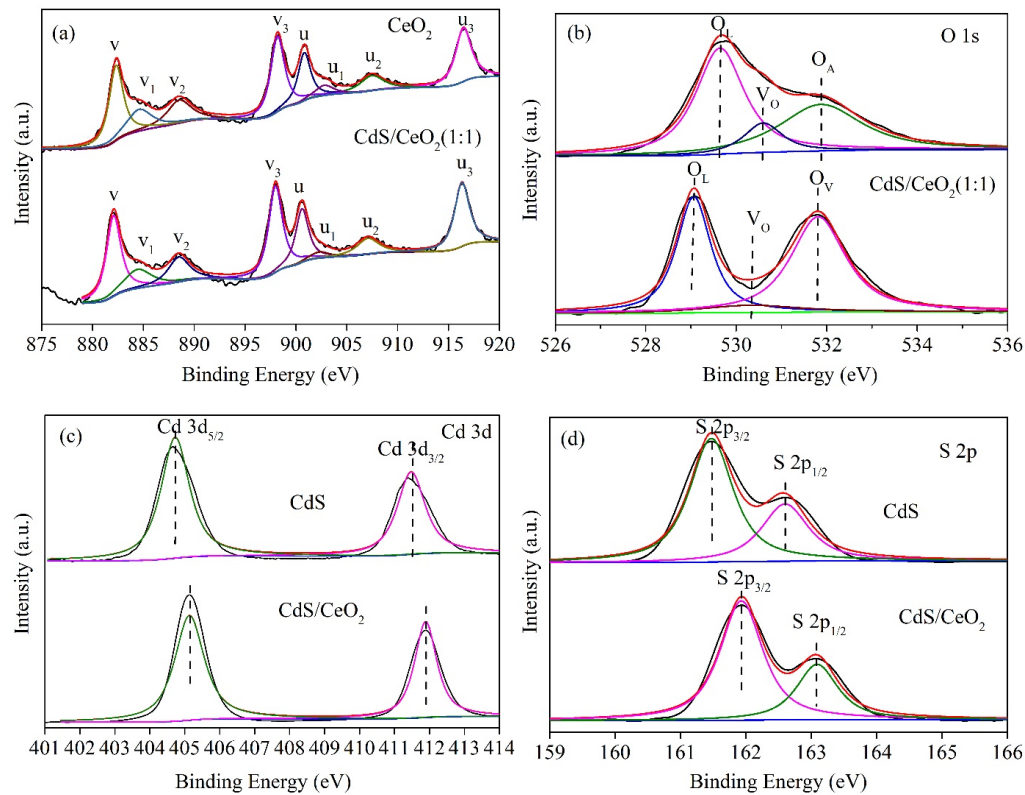


Figure 4. High-resolution XPS spectra (a) Ce 3d, (b) O 1s, (c) Cd 3d and (d) S 2p of the samples.

3.5. UV-Vis DRS Analysis

Figure 5 shows the ultraviolet–visible diffuse reflectance spectra (UV-Vis DRS) of CeO₂, CdS and the CdS/CeO₂ composites. As shown in Figure 5a, the absorption band edge of CeO₂ is about 400 nm, and that of CdS is about 550 nm. For the CdS/CeO₂ composites, the absorption edge is red shifted with the increase in the molar ratio of CdS. According to the Tauc plot of $(\alpha h\nu)^2$ vs. $(h\nu)$, the band gap energy (E_g) values of CeO₂, CdS/CeO₂ (1:2), CdS/CeO₂ (1:1), CdS/CeO₂ (2:1) and CdS are estimated to be 3.1 eV, 2.45 eV, 2.4 eV, 2.36 eV and 2.3 eV (Figure 5b), respectively [32,33]. Therefore, CeO₂ nanorods can only absorb UV light, and the increase in the CdS nanoparticles would result in the increase in light adsorption in the visible region.

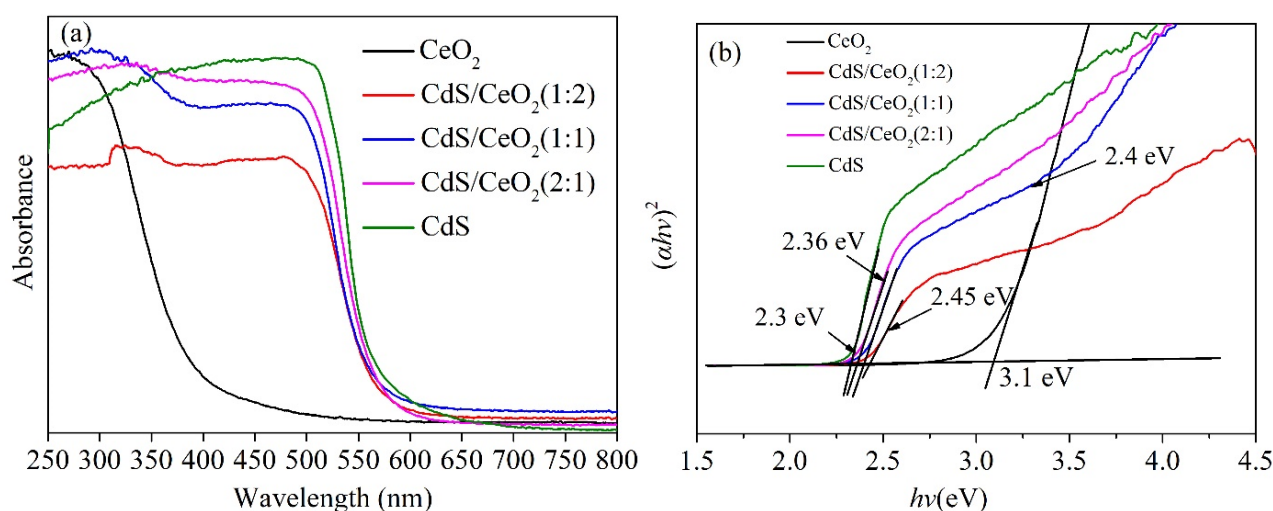


Figure 5. (a) UV-Vis DRS of the photocatalysts; (b) plots of $(\alpha h\nu)^2$ vs photon energy ($h\nu$).

3.6. Performance of Photocatalytic Desulfurization

Figure 6a shows the photocatalytic removal of dibenzothiophene (DBT) from model oil with different photocatalysts. Under dark conditions, all photocatalysts have low desulfurization capacity for DBT. When only H₂O₂ exists without any catalyst, the desulfurization percentage is only about 7.5%, indicating that H₂O₂ has a certain oxidation capacity but the efficiency is relatively low. The photocatalytic desulfurization activities of different samples are as follows: CdS/CeO₂ (1:1) > CdS/CeO₂ (2:1) > CdS > CdS/CeO₂ (1:2) > CeO₂, indicating that the heterojunction formed by CdS and CeO₂ can significantly improve the photocatalytic desulfurization activity. When the molar ratio of CeO₂ and CdS is 1:1, the highest desulfurization efficiency can reach 92% in 3 h. Meanwhile, the corresponding photocatalytic desulfurization kinetic curves over the prepared photocatalysts are shown in Figure 6c. The reaction data are fitted by a first-order model as depicted by the formula [34]: $\ln(C_0/C) = kt + b$, where k is the pseudo-first-order rate constant, and the relationship between $\ln(C_0/C)$ and catalytic reaction time t is considered to be linear. The corresponding desulfurization rate constants (k) are estimated to be 0.08109 h⁻¹, 0.27446 h⁻¹, 0.22957 h⁻¹, 0.57659 h⁻¹ and 0.39763 h⁻¹ for the CeO₂, CdS, CdS/CeO₂ (1:2), CdS/CeO₂ (1:1) and CdS/CeO₂ (2:1). It is clear that the photocatalyst CdS/CeO₂ (1:1) displays the best photocatalytic activity among these prepared photocatalysts. The reusability of the CdS/CeO₂ (1:1) composite is also investigated. As shown in Figure 6c, after repeated use for three times, the desulfurization percentage is about 75%, indicating that the prepared composite has relatively good stability. The desulfurization percentage decreases during the cycle may be attributed to the easy filling of the oxygen vacancy in the photocatalytic process [35].

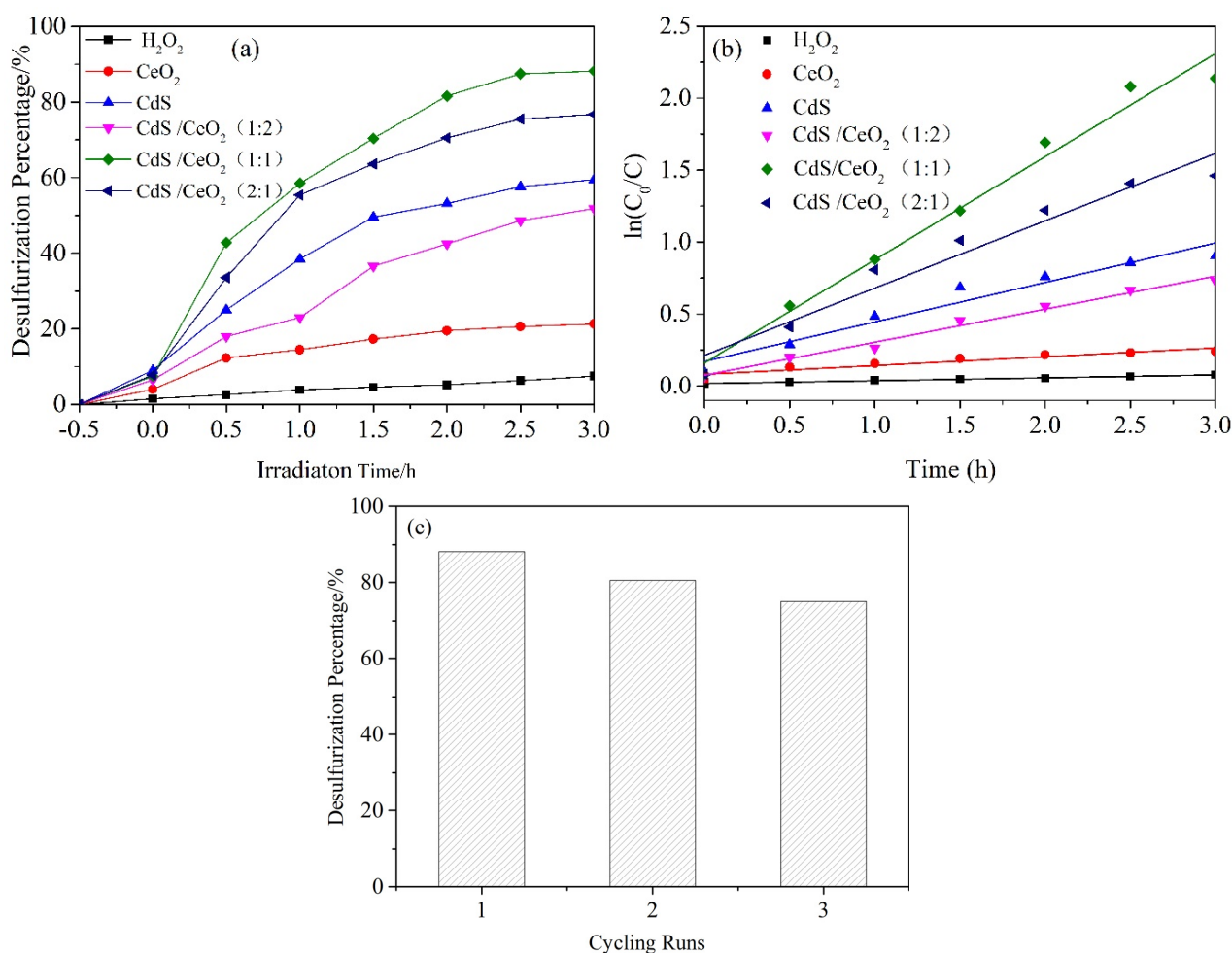


Figure 6. (a) Photocatalytic desulfurization rate of model oil by different photocatalysts; (b) kinetic curves for photocatalytic desulfurization over the prepared photocatalysts; (c) cycling runs of CdS/CeO₂ (1:1) composite on the desulfurization rate.

3.7. Photoelectrochemical and PL Analysis

The photocurrent measurement (PM), electrochemical impedance spectroscopy (EIS) and photoluminescence spectroscopy (PL) are used to analyze photogenerated electrons and holes separation efficiency. As shown in Figure 7a, when the light is turned on, all samples generate photocurrent, indicating that all the samples have light response. It is worth noting that the photocurrent of the CdS/CeO₂ composite sample is significantly higher than that of the pure CeO₂ and CdS, indicating a higher charge separation efficiency [34,36]. The EIS Nyquist plots are displayed in Figure 7b; the arc radius of the CdS/CeO₂ composite sample is obviously smaller than those of the CeO₂ and CdS samples, indicating that the charge transfer resistance of the CdS/CeO₂ composite is lower [37,38]. The PL spectra of CeO₂, CdS and CdS/CeO₂ (1:1) are shown in Figure 7c; the CdS/CeO₂ composite exhibits weaker PL intensity than that of pure CeO₂ and CdS, which indicates that the combination of CeO₂ and CdS can effectively inhibit the recombination of electrons and holes [39,40]. Therefore, the well-defined heterojunction structure is conducive to the transportation and separation of photogenerated electrons–holes, and enhances the photocatalytic activity.

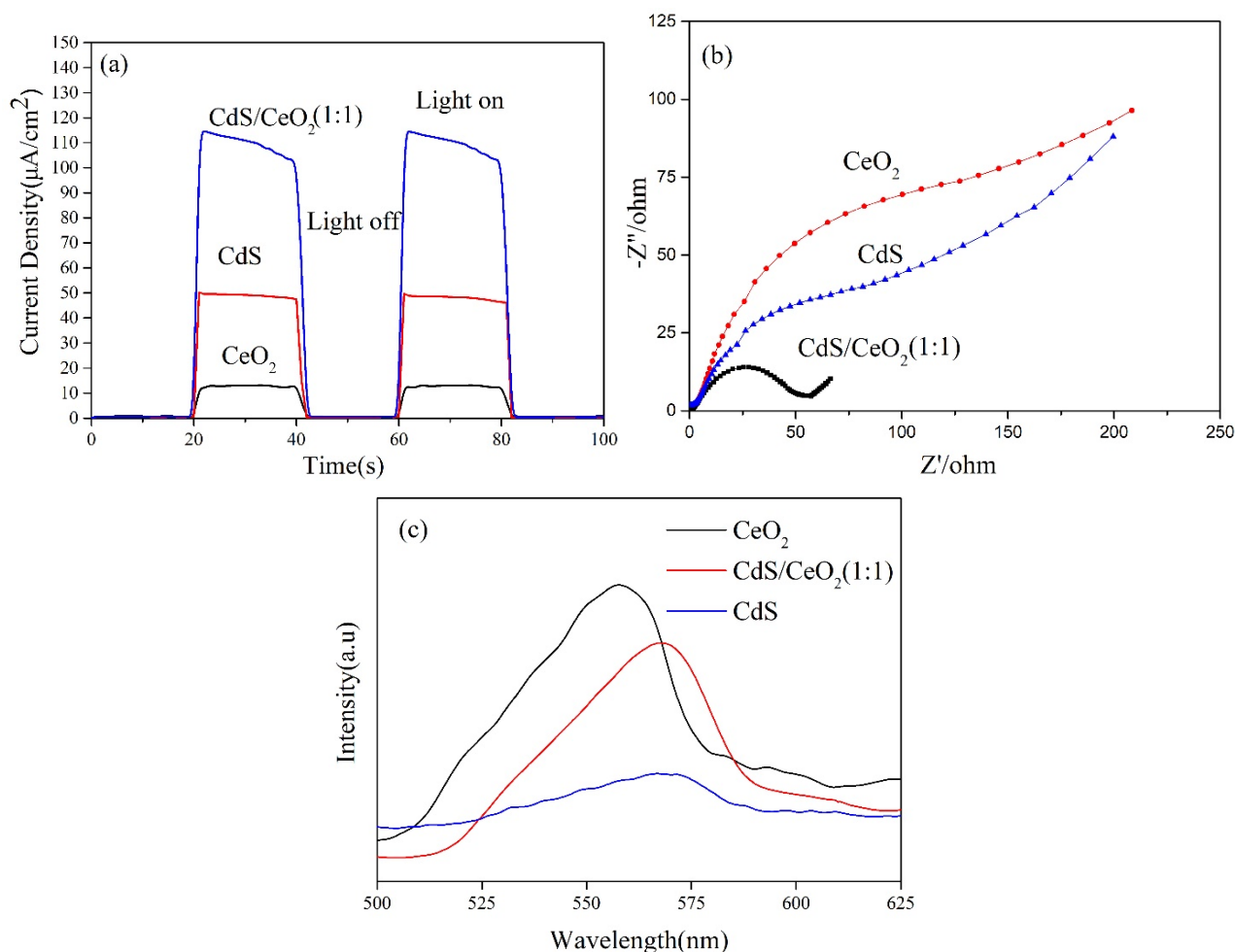


Figure 7. (a) Photocurrent response; (b) Nyquist impedance plots and (c) photoluminescence spectra of CeO₂, CdS and CdS/CeO₂ (1:1).

3.8. Photocatalytic Mechanism

In order to analyze the mechanism of photocatalytic desulfurization, it is necessary to determine the conduction band (CB) and valence band (VB) positions of the semiconductors. The value of the valence band (VB) and conduction band (CB) of the semiconductor can be obtained according to the following formula [37,41]: $E_{CB} = \chi - E_0 - 0.5E_g$, where χ is the electronegativity of a semiconductor, the geometric mean of the electronegativity of the constituent atoms, E_0 is the energy of free electrons on the hydrogen scale (4.5 eV) and E_g is the band gap of the semiconductor. DRS shows that the band gaps (E_g) of CeO₂ and CdS are 3.1 and 2.3 eV, respectively. The calculated CB positions of CeO₂ and CdS are -0.49 and -0.65 eV, respectively, and the calculated VB positions of CeO₂ and CdS are about 2.61 and 1.65 eV, respectively. When the composite is irradiated under visible light, CdS can be activated, and the electrons in the full VB of CdS can migrate to the empty CB, leaving a considerable number of positively charged holes at the corresponding position. Due to the CB potential of CdS (-0.65 eV) being lower than that of CeO₂ (-0.49 eV), the excited electrons in CdS are transferred to the CB of CeO₂ through the heterojunction interface, which leads to the photogenerated electrons (e^-) and holes (h^+) being effectively separated, inhibition of the recombination of photocarriers, and an improvement in the photocatalytic activity. At the same time, the photogenerated electrons react with H₂O₂ to generate hydroxyl radicals (\bullet OH) and hydroxyl (-OH). However, since the VB potential of CdS (1.65 eV) is lower than the redox potential of $-OH/\bullet$ OH (1.99 eV), holes cannot react with hydroxyl (-OH) to form hydroxyl radicals (\bullet OH) [42]. Hydroxyl radicals (\bullet OH) and holes (h^+) with strong oxidation can be oxidized with DBT into DBTO₂. Finally, due to the strong

polarity of DBTO₂, it can be removed by extraction separation to achieve the purpose of desulfurization [2,7,43]. In addition, the surface V_O of CeO₂ plays an important role in the process of photocatalytic desulfurization. It not only serves as an electron reservoir to store the photogenerated electrons and inhibit the recombination of photogenerated electrons and holes, but also acts as an active site to promote the adsorption and activation of H₂O/-OH [29,44]. Figure 8 illustrates the possible photocatalytic desulfurization mechanism.

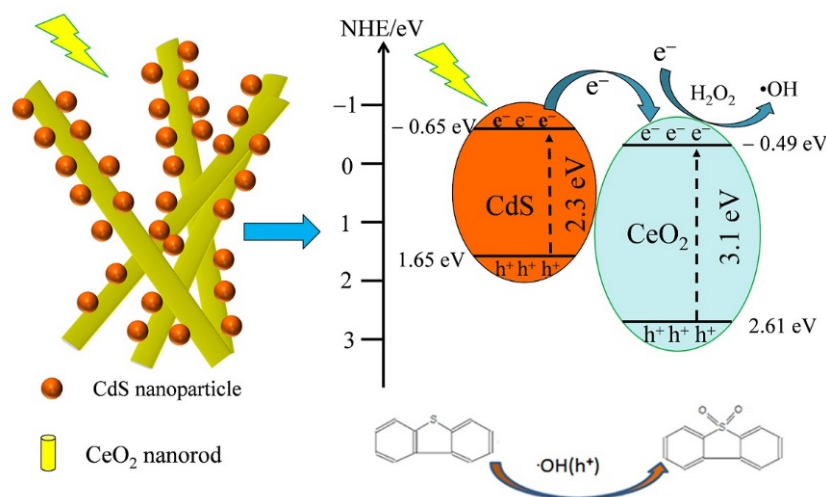


Figure 8. Schematic illustration of photocatalytic desulfurization mechanism of CdS/CeO₂ composite.

4. Conclusions

In conclusion, one-dimensional CeO₂ nanorods were modified by CdS nanoparticles to form a heterojunction photocatalyst. The nanocomposites show great enhanced photocatalytic activity for photocatalytic desulfurization, and CdS/CeO₂ (1:1) shows the highest desulfurization rate of 92% in 3 h under visible light. The nanocomposites demonstrate outstanding photocatalytic activity, and the desulfurization rate reaches 92% for DBT in 3 h. The excellent photocatalytic desulfurization performance is attributed to the transfer of visible light excited electrons on CdS nanoparticles to CeO₂ nanorods, which effectively inhibits the photocorrosion of CdS with narrow band gap and improves the light trapping ability of CeO₂ with a broad band gap. This work may provide a new idea for the design and construction of photocatalytic deep desulfurization materials.

Author Contributions: Conceptualization, X.L. and H.H.; methodology, X.L. and J.Q.; validation, Z.L., X.Z. and H.H.; formal analysis, Z.L., W.X. and H.H.; investigation, X.L. and W.X.; resources, X.L.; data curation, X.Z. and W.X.; writing—original draft preparation, X.L. and Z.L.; writing—review and editing, H.H. and J.Q.; visualization, X.L. and X.Z.; supervision, X.L.; project administration, X.L.; funding acquisition, X.L. and H.H. All authors have read and agreed to the published version of the manuscript.

Funding: This research was supported by Industry-University-Institute Cooperation Project of Jiangsu Province (BY2022428), China; the Funding for school-level research projects of Yancheng Institute of Technology (xjr2019026); and the Natural Science Foundation of the Jiangsu Higher Education Institutions of China (Grant No. 19KJD430008).

Data Availability Statement: Data available on request from the authors.

Conflicts of Interest: The authors declare no conflict of interest.

References

- Lahieb Faisal, M.; Ali, S.A.K.; Al-Sharify, Z.T.; Ali, A. The Effect of Smoke from Factories, Electricity Generator and Vehicles on Human Health and Environment. A Review. *Solid State Technol.* **2020**, *63*, 21390–21398.
- Li, X.Z.; Li, F.H.; Lu, X.W.; Zuo, S.X.; Yao, C.; Ni, C.Y. Development of Bi₂W_{1-x}Mo_xO₆/Montmorillonite nanocomposite as efficient catalyst for photocatalytic desulfurization. *J. Alloys Compd.* **2017**, *709*, 285–292. [[CrossRef](#)]

3. Díaz de León, J.N.; Ramesh Kumar, C.; Antúnez-García, J.; Fuentes-Moyado, S. Recent insights in transition metal sulfide hydrodesulfurization catalysts for the production of ultra low sulfur diesel: A short review. *Catalysts* **2019**, *9*, 87. [[CrossRef](#)]
4. Crucianelli, M.; Bizzarri, B.M.; Saladino, R. SBA-15 anchored metal containing catalysts in the oxidative desulfurization process. *Catalysts* **2019**, *9*, 984. [[CrossRef](#)]
5. Ahmed, I.; Jhung, S.H. Adsorptive desulfurization and denitrogenation using metal-organic frameworks. *J. Hazard. Mater.* **2016**, *301*, 259–276. [[CrossRef](#)]
6. Chen, S.Q.; Zang, M.; Li, L.; Chen, J.T.; Liu, Q.Y.; Feng, X.W.; Sun, S.; Zang, C.W.; Zhao, C.C. Efficient biodesulfurization of diesel oil by *Gordonia* sp. SC-10 with highly hydrophobic cell surface. *Biochem. Eng. J.* **2021**, *174*, 108094. [[CrossRef](#)]
7. Li, X.Z.; Zhu, W.; Lu, X.W.; Zuo, S.X.; Yao, C.; Ni, C.Y. Integrated nanostructures of CeO₂ /attapulgite/g-C₃N₄ as efficient catalyst for photocatalytic desulfurization: Mechanism, kinetics and influencing factors. *Chem. Eng. J.* **2017**, *326*, 87–98. [[CrossRef](#)]
8. Zhou, X.Y.; Wang, T.Y.; Liu, H.; Gao, X.C.; Wang, C.Y.; Wang, G.X. Desulfurization through photocatalytic oxidation: A critical review. *ChemSusChem* **2021**, *14*, 492–511. [[CrossRef](#)]
9. Hitam, C.N.C.; Jalil, A.A.; Triwahyono, S.; Rahman, A.F.A.; Hassan, N.S.; Khusnun, N.F.; Jamian, S.F.; Mamat, C.R.; Nabgan, W.; Ahmad, A. Effect of carbon-interaction on structure-photoactivity of Cu doped amorphous TiO₂ catalysts for visible-light-oriented oxidative desulfurization of dibenzothiophene. *Fuel* **2018**, *216*, 407–417. [[CrossRef](#)]
10. Zhang, G.; Gao, M.; Tian, M.; Zhao, W.F. In situ hydrothermal preparation and photocatalytic desulfurization performance of graphene wrapped TiO₂ composites. *J. Solid State Chem.* **2019**, *279*, 120953. [[CrossRef](#)]
11. Mousavi-Kamazani, M. Cube-like Cu/Cu₂O/BiVO₄/Bi₇VO₁₃ composite nanoparticles: Facile sol-gel synthesis for photocatalytic desulfurization of thiophene under visible light. *J. Alloys Compd.* **2018**, *823*, 153786. [[CrossRef](#)]
12. Ebadi, M.; Asri, M.; Beshkar, F. Novel Mo/Bi₂MoO₆/Bi₃ClO₄ heterojunction photocatalyst for ultra-deep desulfurization of thiophene under simulated sunlight irradiation. *Adv. Powder Technol.* **2021**, *32*, 2160–2170. [[CrossRef](#)]
13. Li, B.L.; Song, H.Y.; Han, F.Q.; Wei, L.S. Photocatalytic oxidative desulfurization and denitrogenation for fuels in ambient air over Ti₃C₂/g-C₃N₄ composites under visible light irradiation. *Appl. Catal. B* **2020**, *269*, 118845. [[CrossRef](#)]
14. Lu, X.W.; Chen, F.; Qian, J.C.; Fu, M.; Jiang, Q.; Zhang, Q.F. Facile fabrication of CeF₃/g-C₃N₄ heterojunction photocatalysts with upconversion properties for enhanced photocatalytic desulfurization performance. *J. Rare Earths* **2021**, *39*, 1204–1210. [[CrossRef](#)]
15. Bagheri, M.; Masoomi, M.Y.; Morsali, A. A MoO₃-metal-organic framework composite as a simultaneous photocatalyst and catalyst in the PODS process of light oil. *ACS Catal* **2017**, *7*, 6949–6956. [[CrossRef](#)]
16. Kusmirek, E. A CeO₂ semiconductor as a photocatalytic and photoelectrocatalytic material for the remediation of pollutants in industrial wastewater: A review. *Catalysts* **2020**, *10*, 1435. [[CrossRef](#)]
17. Wang, A.Q.; Zheng, Z.K.; Wang, H.; Yuwen Chen, Y.W.; Luo, C.H.; Liang, D.J.; Hu, B.W.; Qiu, R.L.; Yan, K. 3D hierarchical H₂-reduced Mn-doped CeO₂ microflowers assembled from nanotubes as a high-performance Fenton-like photocatalyst for tetracycline antibiotics degradation. *Appl. Catal. B* **2020**, *277*, 119171. [[CrossRef](#)]
18. García-López, E.I.; Abbasi, Z.; Parrino, F.; La Parola, V.; Liotta, L.F.; Marci, G. Au/CeO₂ Photocatalyst for the Selective Oxidation of Aromatic Alcohols in Water under UV, Visible and Solar Irradiation. *Catalysts* **2021**, *11*, 1467. [[CrossRef](#)]
19. Liu, J.W.; Zhang, L.; Sun, Y.F.; Luo, Y. Bifunctional Ag-decorated CeO₂ nanorods catalysts for promoted photodegradation of methyl orange and photocatalytic hydrogen evolution. *Nanomaterials* **2021**, *11*, 1104. [[CrossRef](#)]
20. Zhong, Y.; Peng, C.D.; He, Z.T.; Chen, D.M.; Jia, H.L.; Zhang, J.Z.; Ding, H.; Wu, X.F. Interface engineering of heterojunction photocatalysts based on 1D nanomaterials. *Catal. Sci. Technol.* **2021**, *11*, 27–42. [[CrossRef](#)]
21. Alomar, M.; Liu, Y.L.; Chen, W.; Fida, H. Controlling the growth of ultrathin MoS₂ nanosheets/CdS nanoparticles by two-step solvothermal synthesis for enhancing photocatalytic activities under visible light. *Appl. Surf. Sci.* **2019**, *480*, 1078–1088. [[CrossRef](#)]
22. Ning, X.; Lu, G. Photocorrosion inhibition of CdS-based catalysts for photocatalytic overall water splitting. *Nanoscale* **2020**, *12*, 1213–1223. [[CrossRef](#)] [[PubMed](#)]
23. Fang, J.; Bi, X.Z.; Si, D.J.; Jiang, Z.Q.; Huang, W.X. Spectroscopic studies of interfacial structures of CeO₂-TiO₂ mixed oxides. *Appl. Surf. Sci.* **2007**, *253*, 8952–8961. [[CrossRef](#)]
24. Cui, H.J.; Li, B.B.; Zhang, Y.Z.; Zheng, X.D.; Li, X.Z.; Li, Z.Y.; Xu, S. Constructing Z-scheme based CoWO₄/CdS photocatalysts with enhanced dye degradation and H₂ generation performance. *Int. J. Hydrogen Energy* **2018**, *43*, 18242–18252. [[CrossRef](#)]
25. Mani, A.D.; Nandy, S.; Subrahmanyam, C. Synthesis of CdS/CeO₂ nanomaterials for photocatalytic H₂ production and simultaneous removal of phenol and Cr (VI). *J. Environ. Chem. Eng.* **2015**, *3*, 2350–2357. [[CrossRef](#)]
26. Xu, J.; Li, M.; Qiu, J.H.; Zhang, X.F.; Feng, Y.; Yao, J.F. PEGylated deep eutectic solvent-assisted synthesis of CdS@CeO₂ composites with enhanced visible light photocatalytic ability. *Chem. Eng. J.* **2020**, *383*, 123135. [[CrossRef](#)]
27. Maslakov, K.I.; Teterin, Y.A.; Popel, A.J.; Teterin, A.Y.; Ivanov, K.E.; Kalmykov, S.N.; Petrova, V.G.; Petrov, P.K.; Farnan, I. XPS study of ion irradiated and unirradiated CeO₂ bulk and thin film samples. *Appl. Surf. Sci.* **2018**, *448*, 154–162. [[CrossRef](#)]
28. Guo, C.F.; Chen, D.L.; Hu, Y. Perspective on Defective Semiconductor Heterojunctions for CO₂ Photoreduction. *Langmuir* **2022**, *38*, 6491–6498. [[CrossRef](#)] [[PubMed](#)]
29. Ni, M.M.; Zhang, H.Y.; Khan, S.; Chen, X.J.; Chen, F.; Guo, C.F.; Zhong, Y.J.; Hu, Y. In-situ photodeposition of cadmium sulfide nanocrystals on manganese dioxide nanorods with rich oxygen vacancies for boosting water-to-oxygen photooxidation. *J. Colloid Interface Sci.* **2022**, *613*, 764–774. [[CrossRef](#)] [[PubMed](#)]
30. Wang, S.; Zhu, B.C.; Liu, M.J.; Zhang, L.Y.; Yu, J.G.; Zhou, M.H. Direct Z-scheme ZnO/CdS hierarchical photocatalyst for enhanced photocatalytic H₂-production activity. *Appl. Catal. B* **2019**, *243*, 19–26. [[CrossRef](#)]

31. Liu, C.; Zhang, Q.F.; Zou, Z.G. Recent advances in designing ZnIn₂S₄-based heterostructured photocatalysts for hydrogen evolution. *J. Mater. Sci. Technol.* **2022**, *139*, 167–188. [[CrossRef](#)]
32. Makuła, P.; Pacia, M.; Macyk, W. How to correctly determine the band gap energy of modified semiconductor photocatalysts based on UV-Vis spectra. *J. Phys. Chem. Lett.* **2018**, *9*, 6814–6817. [[CrossRef](#)] [[PubMed](#)]
33. Liu, C.; Zhang, Y.L.; Wu, J.X.; Dai, H.L.; Ma, C.J.; Zhang, Q.F.; Zou, Z.G. Ag-Pd alloy decorated ZnIn₂S₄ microspheres with optimal Schottky barrier height for boosting visible-light-driven hydrogen evolution. *J. Mater. Sci. Technol.* **2022**, *114*, 81–89. [[CrossRef](#)]
34. Lu, X.W.; Li, X.Z.; Chen, F.; Chen, Z.G.; Qian, J.; Zhang, Q.F. Biotemplating synthesis of N-doped two-dimensional CeO₂-TiO₂ nanosheets with enhanced visible light photocatalytic desulfurization performance. *J. Alloys Compd.* **2020**, *815*, 152326. [[CrossRef](#)]
35. Li, L.; Guo, C.F.; Ning, J.Q.; Zhong, Y.J.; Chen, D.L.; Hu, Y. Oxygen-vacancy-assisted construction of FeOOH/CdS heterostructure as an efficient bifunctional photocatalyst for CO₂ conversion and water oxidation. *Appl. Catal. B Environ.* **2022**, *613*, 764–774. [[CrossRef](#)]
36. Zhang, Y.; Zhou, H.H.; Wang, H.G.; Zhang, Y.C.; Dionysiou, D.D. Synergistic effect of reduced graphene oxide and near-infrared light on MoS₂-mediated electrocatalytic hydrogen evolution. *Chem. Eng. J.* **2021**, *418*, 129343. [[CrossRef](#)]
37. Lu, X.W.; Li, X.Z.; Qian, J.C.; Miao, N.M.; Yao, C.; Chen, Z.G. Synthesis and characterization of CeO₂/TiO₂ nanotube arrays and enhanced photocatalytic oxidative desulfurization performance. *J. Alloys Compd.* **2016**, *661*, 363–371. [[CrossRef](#)]
38. Zhang, Y.; Hu, L.; Zhang, Y.C.; Wang, X.Z.; Wang, H.G. Snowflake-Like Cu₂S/MoS₂/Pt heterostructure with near infrared photothermal-enhanced electrocatalytic and photoelectrocatalytic hydrogen production. *Appl. Catal. B Environ.* **2022**, *315*, 121540. [[CrossRef](#)]
39. Sun, J.B.; Han, N.; Gu, Y.; Lu, X.W.; Si, L.; Zhang, Q.F. Hole Doping to Enhance the Photocatalytic Activity of Bi₄NbO₈Cl. *Catalysts* **2020**, *10*, 1425. [[CrossRef](#)]
40. Zhang, F.; Zhang, Y.C.; Wang, Y.Y.; Zhu, A.P.; Zhang, Y. Efficient photocatalytic reduction of aqueous Cr (VI) by Zr⁴⁺ doped and polyaniline coupled SnS₂ nanoflakes. *Sep. Purif. Technol.* **2022**, *283*, 120161. [[CrossRef](#)]
41. Guo, X.Y.; Chen, C.F.; Song, W.Y.; Wang, X.; Di, W.H.; Qin, W.P. CdS embedded TiO₂ hybrid nanospheres for visible light photocatalysis. *J. Mol. Catal. A Chem.* **2014**, *387*, 1–6. [[CrossRef](#)]
42. Lu, X.W.; Quan, L.M.; Hou, H.J.; Qian, J.C.; Liu, Z.W.; Zhang, Q.F. Fabrication of 1D/2D Y-doped CeO₂/ZnIn₂S₄ S-scheme photocatalyst for enhanced photocatalytic H₂ evolution. *J. Alloys Compd.* **2022**, *925*, 166552. [[CrossRef](#)]
43. Wang, C.; Zhu, W.S.; Xu, Y.H.; Xu, H.; Zhang, M.; Chao, Y.H.; Yin, S.; Li, H.M.; Wang, J.G. Preparation of TiO₂/g-C₃N₄ composites and their application in photocatalytic oxidative desulfurization. *Ceram. Int.* **2014**, *40*, 11627–11635. [[CrossRef](#)]
44. Xiong, J.; Di, J.; Xia, J.X.; Zhu, W.S.; Li, H.M. Surface defect engineering in 2D nanomaterials for photocatalysis. *Adv. Funct. Mater.* **2018**, *28*, 1801983. [[CrossRef](#)]